Research Article
Vol. 29, No. 7 / 29 March 2021 / *Optics Express* 10780

Optics EXPRESS

Inverse design of a single-frequency diffractive biosensor based on the reporter cleavage detection mechanism

HAEJUN CHUNG[1,2] AND **SVETLANA V. BORISKINA**[1,3]

[1] *Department of Mechanical Engineering, Massachusetts Institute of Technology, Cambridge, MA 02139, USA*
[2] *haejun@mit.edu*
[3] *sborisk@mit.edu*

Abstract: Vertically interrogated porous silicon (PSi) interferometric biosensors have shown high potential for sensing bio-molecules as they combine high detection sensitivity with simplicity of fabrication, functionalization, optical coupling, and interfacing with microfluidic systems. However, most interferometric sensor designs require either broadband or wavelength-tunable light sources as well as wide-angle detection schemes, increasing their complexity and cost for point-of-care biosensing applications. The limit of detection of such sensors is also constrained by the small size and low refractive index of biological molecules, making it hard to detect very low concentrations of pathogens. In this work, we use a large-scale computational "inverse design" technique to demonstrate a single-frequency, fixed-angle PSi-based biosensor, which exploits a recently developed high-contrast reporter cleavage detection (HCCD) technique. The HCCD sensors detect high-index reporter cleavage events instead of low-index target analyte capture events as typical for traditional label-free optical biosensors. We use the inverse design approach to discover an optimal configuration of a PSi biosensor that makes use of the extended achievable range of cleavage-induced PSi effective index variations and can be interrogated at a single frequency and at a fixed angle. The optimized design in the form of a one-dimensional PSi grating exhibits the change in the reflectance up to 55 % at the interrogation angle of 12° and wavelength of 600 nm, which is caused by cleavage of Au nanoparticle reporters initially occupying 2% of the sensor surface area. The maximum possible change in reflectance is predicted to be 222 % (for a two-dimensional freeform design not amenable to fabrication). This demonstration may pave the way for developing new or redesigned conventional interferometric and colorimetric point-of-care biosensor systems in combination with the cleavage-based detection schemes.

1. Introduction

Porous silicon (PSi)-based optical biosensors have demonstrated great potential for applications in commercialized real-time sensing of biomolecules [1–11]. PSi offers a variety of advantages in optical biosensing, including extremely large surface area, fabrication simplicity, and well-developed surface chemistry for device functionalization with receptors to capture biological molecules [12]. Many practical PSi biosensor platforms have been developed, including single-layer interferometers [13,14], Bragg mirrors [15], microcavities [6], Rugate filters [5], diffraction gratings [9,16,17], ring resonators [4], and colorimetric sensors [18]. The PSi-based optical biosensor design approaches have recently evolved towards engineering relatively high-quality factor photonic devices capable of detection of very small changes of refractive indices caused by the capture of target bio-molecules [4,12]. However, it opens a new challenge, where a small noise can be also amplified in a high-quality factor design. These includes the spectral noise due to the limited spectral resolution of both the laser and the optical detection system, thermal variations, and the indiscriminate molecular binding events [19,20]. While the effect of the

#421656
Journal © 2021
https://doi.org/10.1364/OE.421656
Received 4 Feb 2021; revised 9 Mar 2021; accepted 11 Mar 2021; published 22 Mar 2021

thermal noise can be reduced by referencing or self-referencing the biosensor [21,22], increasing spectral resolution of the system also increases its cost and complexity, and the indiscriminate binding events are hard to avoid when working with biological molecules.

On the other hand, low-quality factor optical biosensor designs can still achieve low detection limits provided they can be engineered to achieve high sensitivity to the refractive index changes in the environment [19,23]. The diffraction grating is a particularly interesting low-quality-factor optical biosensor system, because it only requires a single frequency light source and a photodetector, eliminating the need for complicated broadband high-spectral-resolution signal processing, which could have a great advantage in developing a simple real-time point-of-care sensing systems. Two types of grating-based biosensors have been previously proposed and investigated. A grating-coupler waveguide approach uses the angular-dependent response of the grating coupler, where light incident at the critically-matched angle creates a strong resonance in the reflectance signal [9]. On the other hand, a diffraction-grating approach is based on measuring the changes in the intensity of light reflected at a fixed wavelength and into a fixed angle as a result of light diffraction on a grating structure [24,25]. The latter approach only requires a single-frequency or a narrowband light source illuminating the grating at a fixed angle, and a single photo-detector to measure the reflected signal, making it a great candidate for the simplest design of a point-of-care biosensor.

However, creating clear distinct diffraction intensities for the biosensor response corresponding to the positive and negative test results has been very challenging due to a low refractive index of biological molecules and the difficulty of designing multi-state diffractive optical devices. Recently, we have proposed and experimentally demonstrated the High-Contrast Cleavage Detection (HCCD) technique on a porous silicon platform, proving that the change of the refractive index of the PSi biosensor can be increased significantly if the conventional biomolecule capture detection mechanism is replaced with the high-contrast reporter cleavage mechanism [26,27]. The new mechanism makes use of the biosensor surface functionalization with high-index nanoscale reporters (e.g., quantum dots, semiconductor or noble-metal nanoparticles), which are then cleaved from the surface by a cleaving agent (e.g. a CRISPR complex) activated by the target biomolecule. [26,27]. In this work, taking advantage of the HCCD mechanism, we use a large-scale computational optimization approach called “inverse design" to engineer and optimize a highly-efficient diffraction grating that has a distinctly different optical response in the negative- and positive-result states (i.e., corresponding to the sensor effective refractive index values before cleavage and after cleavage of high-contrast reporters). The optimized diffraction grating shows 222 % (2D freeform) and 55 % (1D grating) intensity changes with a single-frequency light incident and detected at a fixed angle, 12° (2D freeform) and 24° (1D grating). Furthermore, the far-field intensity of the diffraction changes linearly with the number of the cleaved probes, which can be used to monitor the kinetics of the cleavage processes and to estimate the number of target molecules in the sample. This simple grating-type sensor, which can be easily re-designed for other porous materials such as e.g., anodized alumina or porous polymers, can be used to develop a simple and low-cost optical biosensor system for the point-of-care detection of known and emerging pathogens, including SARS-CoV-2 virus.

2. Inverse design

Figures 1(a)-(c) shows a schematic depiction of the HCCD biosensing approach and its integration with the inverse-designed diffraction-grating PSi biosensor. The grating structure to be optimized is composed of the nanostructured PSi layer backed by the distributed Bragg reflector (DBR) dielectric mirror to achieve efficient reflectance of incident light while minimizing the mirror dissipative losses. The DBR mirror composed of TiO_2 and SiO_2 layers has been optimized to exhibit an optical bandgap centered at the operating wavelength of 600 nm (cf. Appendix for the detailed design parameters). The Bragg mirror offers high reflection with a negligible parasitic absorption while a Si substrate offers a simple fabrication process but higher parasitic absorption and lower reflection. The other alternative is a metallic mirror, which offers high reflectivity. We believe that other types of back reflectors mentioned above may work very well with our proposed inverse design scheme, but they may have slightly lower efficiency due to lower reflectance and/or parasitic absorption. In its initial state shown in Fig. 1(b), the biosensor PSi surface is functionalized by high-contrast nanoparticle (NP) reporters (e.g., quantum dots or metal nanoparticles), attached to the sensor by the deoxyribonucleic acid (DNA) or ribonucleic acid (RNA) tethers. The surface functionalization with the reporters can be achieved by using well-known hierarchical organic molecule layers, such as e.g., (3-Aminopropyl)triethoxysilane (APTES)-glutaraldehyde-streptavidin molecular complexes in the case of silicon and glass sensor surfaces [28,29]. After sensor exposure to the target biomolecule in the presence of cleaving agents (e.g., CRISPR-Cas12a complexes [30]), some of the reporters are collaterally cleaved by the activated agents and can be washed away (Fig. 1(c)). This results in the changes of the effective refractive index of the PSi material in the sensor final (positive-result) state. In the case of the negative result, when no target biomolecule is present in the tested sample, the reporter cleavage does not happen, and the refractive index of the sensor does not change. HCCD mechanism offers an opportunity to achieve a significant effective refractive index change by making use of the collateral cleavage of multiple reporters by an agent activated by a single target biomolecule [31,32].

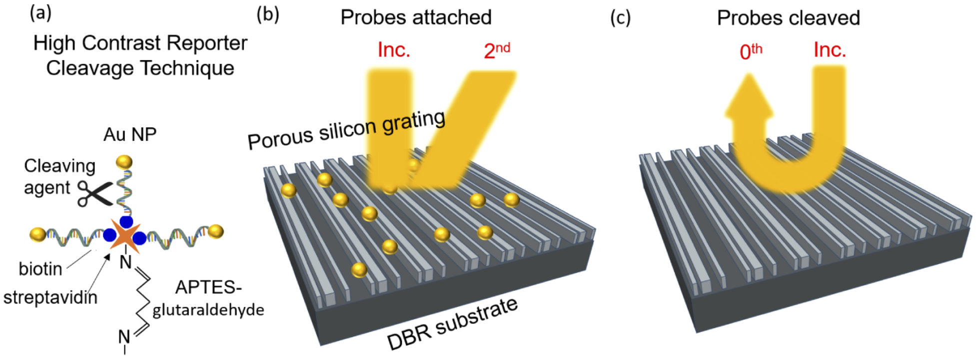

Fig. 1. Schematic figures showing (a) high contrast cleavage detection (HCCD) technique, (b) a porous silicon grating on a distributed Bragg reflector (DBR) substrate functionalized with the Au NP reporters, (c) the grating after the target-molecule-activated reporter cleavage. The dominant diffraction order changes from 2_{nd} to 0_{th} order after reporter cleavage.

Nevertheless, designing a high-efficiency two-state diffraction grating is still challenging due to the lack of a well-developed universal design methodology for multi-state diffraction gratings engineering. Furthermore, the effective refractive index change of the PSi material may still not be significant enough even when large number of reporters is cleaved. For example, freshly fabricated porous Si layer with 70 % porosity exhibits an effective refractive index of 1.637 at the wavelength of 600 nm. This estimate is based on the Bruggeman's model using the silicon's refractive index (n_{Si}) of 3.948 at 600 nm, and confirmed by experiments [26]:

$$(1-\rho)\cdot\frac{n_{Si}^2-n_e^2}{n_{Si}^2+2n_e^2}+\rho\cdot\frac{1-n_e^2}{1+2n_e^2}=0, \tag{1}$$

where ρ is the porosity, n_e is the effective refractive index of the PSi layer, and the void space refractive index is 1 for air.

The oxidation of silicon significantly lowers the PSi layer refractive index (e.g., the effective index value of the oxidized silicon layer (30% oxidized silicon/70% air) of 1.480 has been experimentally estimated [26]). The effective refractive index of the oxidized porous Si layer is further progressively reduced with the increased porosity of the material (see Eq. (1)). Finally, attachment of organic molecules to tether the reporters to the sensor surfaces further slightly increases the effective refractive index of the multi-material porous layer. For example, we have recently reported the final effective refractive index value of the PSi layer with 73% initial porosity to be as low as 1.2849 [26] after oxidization.

Since functionalized PSi has a significantly lower refractive index value than the materials typically used to create diffraction gratings (e.g., metals or high-index semiconductors), it is non-trivial to design even a single-state diffraction grating with any of the commonly-used design methods, including the geometric phase-gradient method [33,34], blazed grating method [35], and unit-cell optimization [36,37]. Other porous dielectric materials such as e.g. anodized alumina or porous polymers, will have even lower effective refractive indices [38].

To address this challenge, we apply the inverse design method to engineer a two-state diffraction grating with the low index material. Inverse design computes gradients with respect to structural degrees of freedom by "adjoint" calculation. This approach has been adapted from control theory [39–42], circuit theory [43], mechanics [44], aerodynamics [45], and deep learning [46–48] in the form of "backpropagation". Recently, it has been introduced to nanophotonics and used to engineer and optimize waveguide demultiplexers [49–51], photonic bandgap structures [52], beam deflectors [53,54], solar cells [55], and tunable metasurfaces [56]. This method offers great advantage in designing multi-state metasurfaces, because it can simultaneously average over the figure of merits for multiple states [56]. The key metric of the optimization can be described as:

$$\mathcal{F}(g) = \frac{1}{2}\sum_{s=\mathrm{a,b}}\left[P^{s}_{\mathrm{tar}}(g) - \sum_{j\neq \mathrm{tar}} P^{s}_{j}(g)\right], \tag{2}$$

where $P^{s}_{\mathrm{tar}}(g)$ is the power in the target (desired) diffraction orders, s denotes the grating state, $P^{s}_{j\neq}(g)$ is the simulated power in j_{th} diffraction order, and g denotes a geometric degree of freedom. Minimizing the figure of merit yields the optimum structure that switches the diffracted light from $j_{\mathrm{th}}(s = a)$ order to $j_{\mathrm{th}}(s = b)$ order. The diffraction power can be calculated with a plane-wave decomposition at the reflection side by using a total-field scattered-field technique [57]. The plane-wave decomposition is given by

$$\boldsymbol{E}(\boldsymbol{x})_{\mathrm{scat.}} = \boldsymbol{E}(\boldsymbol{x})_{\mathrm{total}} - \boldsymbol{E}(\boldsymbol{x})_{\mathrm{inc.}} = \frac{1}{A}\sum_{j} c_j \hat{\boldsymbol{\varepsilon}}_j e^{i\boldsymbol{k}_j\cdot\boldsymbol{x}}, \tag{3}$$

where $\boldsymbol{k}_j$ the wavevector of each plane wave, j a discretized order comprising the angle and the polarization of light, and $\hat{\boldsymbol{\varepsilon}}_j$ is the polarization unit-vector in Eq. (3). Then, the diffraction power is P_j is

$$P_j = \frac{A}{2Z_0}|c_j|^2\,\mathrm{Re}(\boldsymbol{k}_j/\boldsymbol{k}_0), \tag{4}$$

where Z_0 is the optical impedance at the decomposition plane, k_0 is the wavenumber at the decomposition plane in Eq. (4). Note that $\boldsymbol{k}_j$ will be purely imaginary for evanescent orders, such that $\mathrm{Re}(\boldsymbol{k}_j) = 0$ for these orders. The adjoint current source is given by $\boldsymbol{J}_{\mathrm{adj}} = -i\omega\boldsymbol{P}_{\mathrm{adj}} = -i\omega\partial\mathcal{F}/\partial\boldsymbol{E}$ (Ref. [58]).

As illustrated in Figs. 1(b) and (c), the initial and the positive-test final states of our biosensor are chosen as (1) a PSi layer functionalized with gold (Au) nanoparticle-labeled reporters anchored to the Si surfaces by DNA or RNA tethers [27] and (2) a PSi layer after the Au nanoparticle reporters have been cleaved from its surface as a result of the exposure to the target biomaterial that activates the cleaving agent. The detailed measurement and estimation of the effective refractive indices of the initial and the final states can be found in the previous work [27] and

Appendix. In the case of the negative test result, the initial state of the diffraction grating is not expected to change.

We use MEEP [59], open-source finite-difference time-domain method, to calculate forward and adjoint simulations of the biosensors. We employ Bloch boundary conditions at the edges of the FDTD unit cell and the transverse magnetic plane wave as the excitation optical field.

3. Diffractive biosensor optimization

We first explore an optimal design in the 2D freeform structure where we do not impose any structural constraint except the minimum feature size (30 nm). This will allow us to estimate the best theoretically achievable device performance under the HCCD sensing scenario. We assume a two-dimensional structure with a unit-cell periodicity of 4.8 λ (2.88 μm) and a thickness of 1.5 λ (0.9 μm) as shown in Figs. 1(b) and (c). The structure periodicity was chosen to be large enough to secure enough degrees of freedom for the optimization procedure while allowing accurate and efficient FDTD calculations of the unit cell optical response. At the same time, the first and second diffraction orders associated with this larger periodicity have diffraction angles greater than 10°, which ensures that the far-field diffraction pattern can be resolved clearly. The values of the dielectric permittivities used in this study are taken from prior experimental measurements, and include: silicon [60], Au [60], and biomaterials used to tether the Au nanoparticles to the sensor surface (APTES [61], glutaraldehyde [62] streptavidin [63]), respectively. The illuminating optical field has been chosen in the form of a transverse magnetic plane wave incident normally to the sensor surface. Although we use a 30-nm grid spacing (λ/20), the optimized structures have been validated up to (λ/120) grid-spacing to ensure numerical convergence of the algorithm (cf. Appendix).

Figure 2 shows an optimized 2D freeform PSi biosensor. The dominant order switches from 1_{st} order to 0_{th} order if the nanoparticle reporters are cleaved from the sensor surface. At the 0_{th} order reflection angle, the calculated field intensity change is from 22 % to 66 %, while at the 1_{st} order angle it changes from 58 % to 18 %. Note that this change is observed at the constant wavelength of 600 nm, thus there is no need for measuring and processing broadband reflectance spectra to capture either resonance frequency shifts or complicated phase changes. Figure 2(b) demonstrates inverse design iterations and the corresponding intermediate structures. The effective refractive indices of the PSi layer (1.0 % Au volume fraction) are estimated to be 1.2849 (after cleavage), 1.2470 (before cleavage), respectively. The structure at the fifth iteration shows an intermediate multi-layer-type geometry in grayscale, which may greatly improve total reflectivity due to DBR-like behavior, while creating different reflection fields for the two sensor states. From the 20_{th} iteration to the final iteration, the intermediate geometry gradually becomes a binary structure with a penalization method [64]. The final structure has a disconnected multi-layer type geometry combined with 2D freeform objects. This freestanding structure is impossible to fabricate, but it provides an estimate of the theoretical optimization range, which is large enough to make possible engineering practical PSi gratings making use of the HCCD mechanism. Realistic structures with the switching response within this range can then be optimized by imposing additional constrains to the structure geometry.

To reveal the physical mechanism that drives the diffraction order switching caused by a small index change in the inverse-designed structure, we calculated the field intensity distribution (cf. Appendix, Fig. 10) and the near-field optical powerflow patterns inside the PSi layer. The optical powerflow pattern is illustrated by plotting the intensity and the phase distribution of the Poynting vector as shown in Appendix Fig. 10 and Fig. 2(d), respectively. By comparing the Poynting vector phase distributions before and after the cleavage event, it can be seen that prior to cleavage, the near-field interference field features multiple optical vortices (i.e., areas or optical powerflow circulation forming around the phase singularities - points of total destructive interference of the electromagnetic field) [65–68]. The small change in the effective refractive index caused by

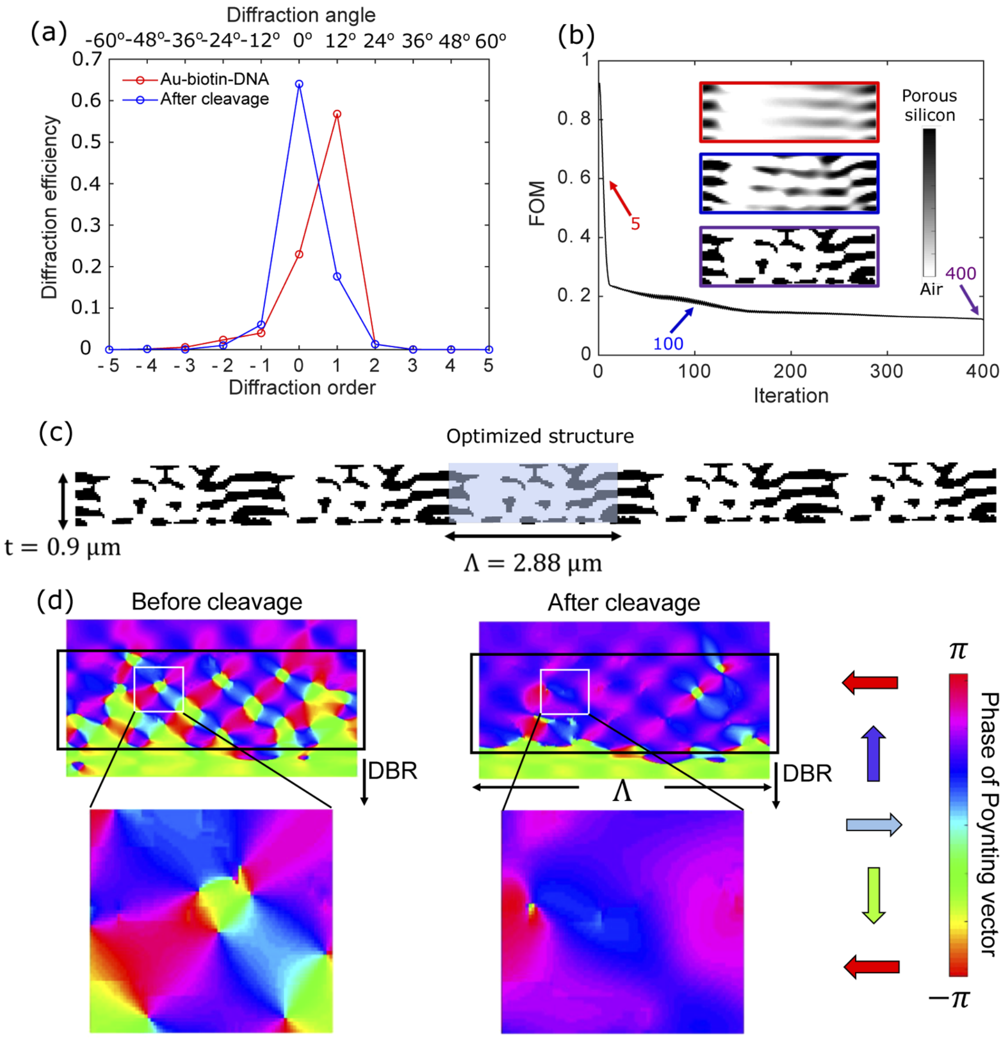

Fig. 2. Optimization of a porous silicon grating via inverse design at 600 nm wavelength. (a) Diffraction efficiency of the optimized device at 600 nm wavelength. The target order diffraction shows 58 % (with probes attached) and 65 % (after cleavage). The unwanted order diffractions are minimized via the FOM defined in this work. (b) Inverse design iteration versus figure of merit defined in Eq. (2). The inset figures show intermediate structures in the inverse design iteration. Porous silicon in the color bar indicates an oxidized porous silicon with initial porosity of 73%, which has refractive index of 1.2849. (c) The optimized final 2D freeform design of the porous silicon sensor. The period of the structure is 4.8 λ long (2.88 μm) and thickness is 1.5 λ (0.9 μm). (d) The optical powerflow pattern in the sensor near field (quantified by plotting the phase distribution of the Poynting vector) features multiple optical vortex pairs across the designable region (black solid line), with some vortex pairs shown in more detail by zooming into a small region enclosed by a white rectangle. The colored arrows indicate the direction of the local powerflow for each corresponding color.

the probes cleavage is however large enough to change the interference pattern and annihilate most of the vortex pairs, while re-positioning others. This causes drastic changes in the near-field optical powerflow pathways, and, in turn, results in the switching of the diffraction order in the far field of the sensor. These large variations of the optical response of the structure caused by a relatively small perturbation stem from the topological nature of optical vortices, which appear or annihilate in pairs, causing major re-distribution of the powerflow as a result of the vortex emergence or annihilation events.

We used a realistic fabrication constraint by reducing the acceptable sensor designs to the two dimensional ridge-type grating structures composed of ridges of constant height and minimum width of 30 nm, distributed on the surface without any wavelength-scale periodicity required. The optimal device, shown in Fig. 3, has the thickness of 0.54 μm and the same large-scale (i.e., FDTD unit cell) periodicity as the 2D freeform structure. Unlike the case of a 2D freeform design, the greater designable volume is not necessarily beneficial for optimizing a realistic grating structure for the highest efficiency. Therefore, we chose the thickness of the PSi grating such that it will be amenable to fabrication by standard lithographic techniques. The effective refractive indices of the PSi layer (2.0 % Au volume fraction) are estimated to be 1.2849 (after cleavage), 1.2133 (before cleavage), respectively. The optimal device shown in Fig. 3(a) has the grating thickness of 540 nm and exhibits switching of the reflected light from 2_{nd} order to 0_{th} order upon cleavage of the nanoparticle-labeled reporters. At the 0_{th} order reflection angle, the intensity change is from 24 % to 47 % while at the 2_{nd} order angle it changes from 42 % to 27 %.

To relate this diffraction efficiency to the real experiment using a single-frequency laser light as the excitation field instead of a planewave, Figs. 3(d) and (e) demonstrate the far-field optical field intensity profile under the Gaussian beam incidence. The intensity switching between the 2_{nd} order and 0_{th} can be clearly seen without any post-processing method. The optimal structure shown in Fig. 3(c) is composed of two repeating similar structures (they are off by one parameter) within the given periodicity (2.88 μm). This effect makes the diffraction powers being concentrated on the even diffraction orders (-4, -2, 0, 2, 4), whose angles match with a -2,-1,0,+1,2 orders of the half-periodicity (1.44 μm). Figure 3(b) demonstrates the inverse design iterations and the corresponding intermediate structures.

Similar to the case of the freeform structure design, we investigated the changes in the near-field optical powerflow pattern than drive the observed changes in the far-field diffraction pattern. The Poynting vector phase profile shown in Fig. 3(f) features a few optical phase singularities with the associated optical vortices driving the powerflow in the near field of the grating. Upon cleavage, some of this singularities shift and annihilate each other, resulting in the switching of the grating far-field diffraction pattern. Note that a similar vortex-driven optical switching mechanism is behind phase transitions of hyperbolic metamaterials [68], plasmonic nanolensing effect [69,70], and the enhanced light transmission through plasmonic nanohole arrays [65].

Although both the 2D freeform and the 1D grating optimized configurations demonstrate promising sensing performances, attaching the exact number of probes could be very challenging experimentally [26]. Thus, we evaluate the device sensitivity to the variations in the surface functionalization coverage by calculating the far-field field intensity profiles for different volume fractions of the Au probes in the PSi material, as shown in Fig. 4. The optimized grating was designed with the assumption of 2.0 % Au volume fraction before cleavage. Our calculations show that for different Au volume fractions ranging from 1.5 % to 2.5 %, the far-field intensity varies linearly, which makes it possible to predict the initial volume fraction of Au probes by analyzing the intensity profiles. This observation proves that the optimized diffraction grating design proposed here can tolerate fabrication imperfections and varied reporter surface coverage densities, and may potentially lead to a development of biosensor capable of monitoring the probe cleavage events in real time.

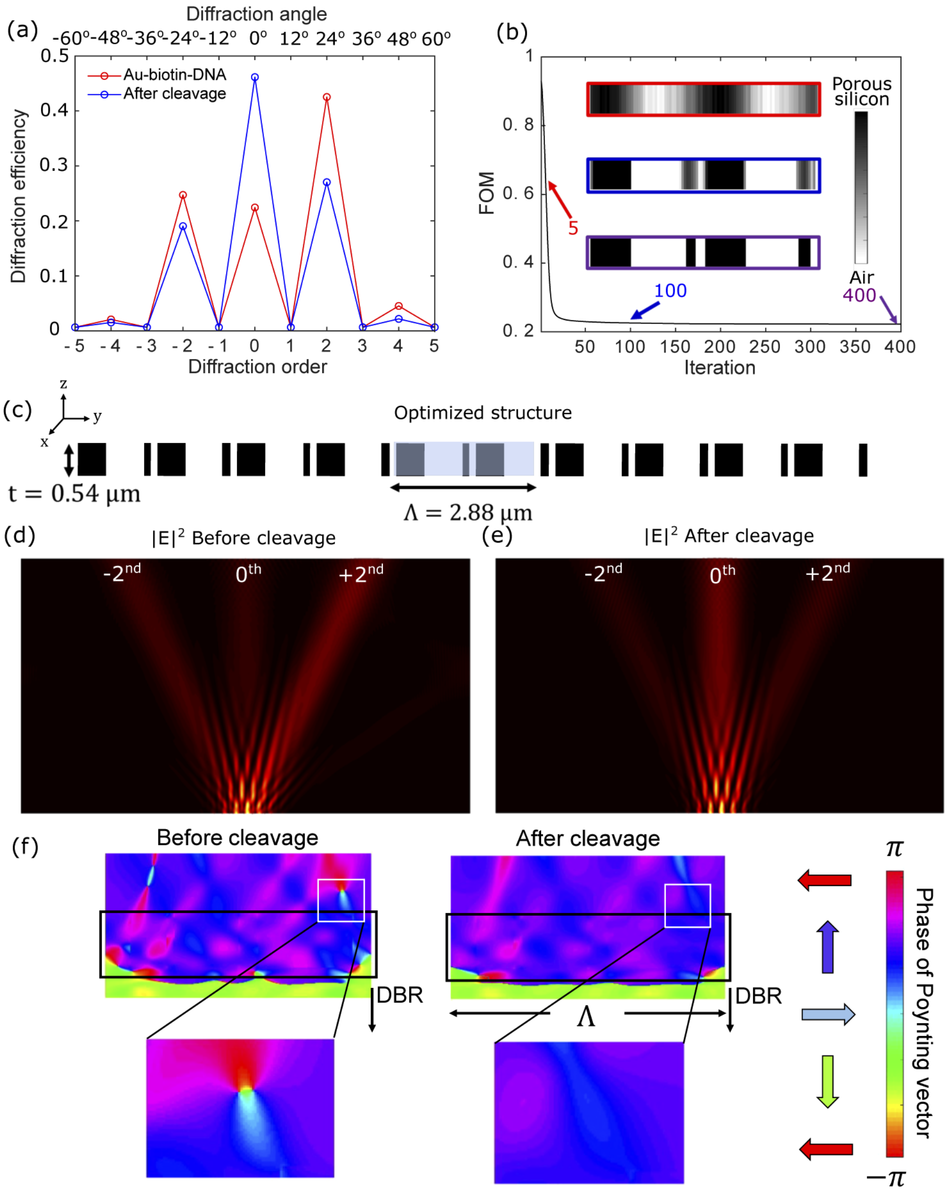

Fig. 3. Optimization of a porous silicon biosensor via inverse design at 600 nm wavelength with a 1D grating structure. (a) Diffraction efficiency of the optimized device at 600 nm wavelength. The target order diffraction shows 42 % (before cleavage) and 47 % (after cleavage). (b) Evolution of the figure of merit defined in Eq. (2) as a function of the number of design iterations. The inset figures shows an intermediate structure in the inverse design iteration. (c) The optimized structure showing the 1D grating design of the porous silicon structure. The period of the structure is 4.8 λ long (2.88 μm) and thickness is 0.9 λ (0.54 μm). E-field intensity profile under the unfocused Gaussian beam incidence before cleavage (d) and after cleavage (e). (f) The phase distribution of the Poynting vector features a few vortex pairs across the designable region (black solid line). The colored arrows indicate the direction of the local powerflow for each corresponding color.

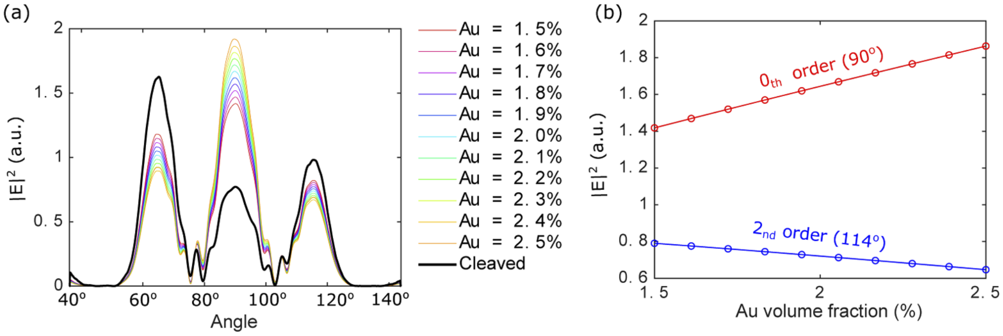

Fig. 4. (a) Far-field intensity distribution for various Au probes volume fractions and angles. (b) 0_{th} (90°) and 2_{nd} (114°) intensity changes over different Au volume fractions.

4. Summary and outlook

In this work, we have demonstrated an inverse design approach to develop a new diffractive-type single-frequency fixed-incidence angle porous silicon biosensing platform with the vertical optical readout mechanism suitable for real-time point-of-care applications. We focused on grating-like designs in 2D with two schemes (2D freeform and 1D grating). The former configuration provided an estimate for the upper limit of the sensing performance, while the latter yielded a lithography-compatible practical sensor geometry with a linear intensity change expected as a result of the probe cleavage. We attribute the switchable behavior of the inverse-designed sensors to the proper engineering of the near-field optical powerflow patterns driven by optical vortices, which are re-configured as a result of the probe cleavage event. A natural extension of this work would be to implement an inverse design technique in combination with the high contrast reporter cleavage detection approach to inverse-design an on-chip integrated interferometric sensor platform to further simplify optical readout mechanism in a compact portable sensor configuration. The new types of inverse-designed sensor platforms making use of the HCCD mechanism hold high promise for the development of simple yet accurate point-of-care biosensors, which are easily programmable for detection of different pathogens, including SARS-Cov-2 virus.

5. Appendix

In the Appendix, we will discuss the convergence study (Figs. 5, 6, and 7), the robustness study (Figs. 8 and 9), and the phase analysis of the Poynting vector (Figs. 10 and 11).

5.1. Convergence study

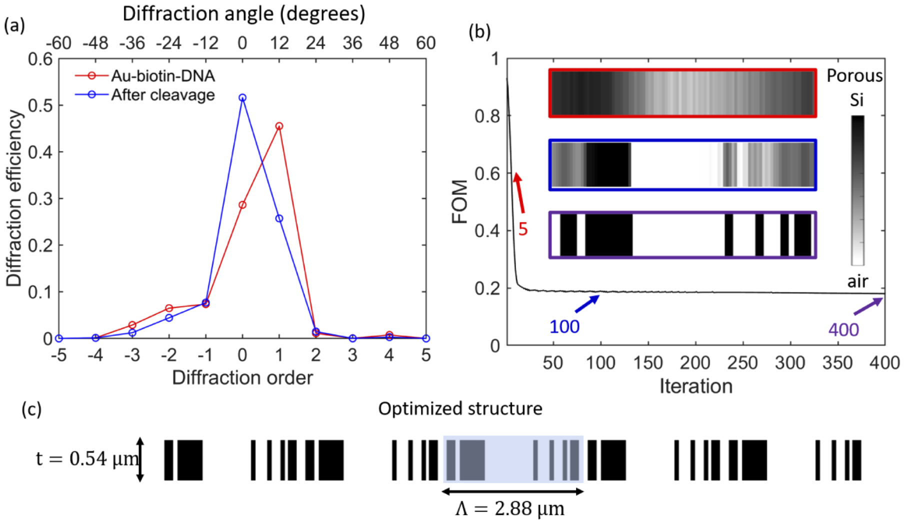

Fig. 5. Optimization of a porous silicon biosensor via inverse design at 600 nm wavelength with 1D grating structure for a convergence check. (a) Diffraction efficiency of the optimized device at 600 nm wavelength. The target order diffraction efficiencies are 47 % (1_{st} order, before cleavage) and 52 % (0_{th} order, after cleavage). (b) Inverse design iteration versus figure of merit defined in Eq. (1) of the main article. The inset figures show intermediate structures in the inverse design iteration. (c) The final optimized structure showing freeform design of the porous silicon diffractive biosensor platform. The period of the structure is 4.8 λ (2.88 μm) and thickness is 0.9 λ (0.54 μm).

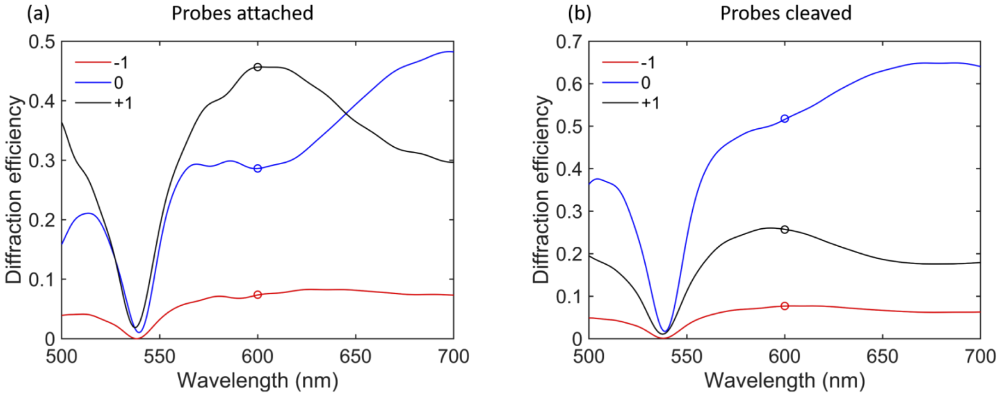

Fig. 6. Broadband response of the optimized biosensor in Fig. 5. (a) Probes attached, (b) Probes cleaved.

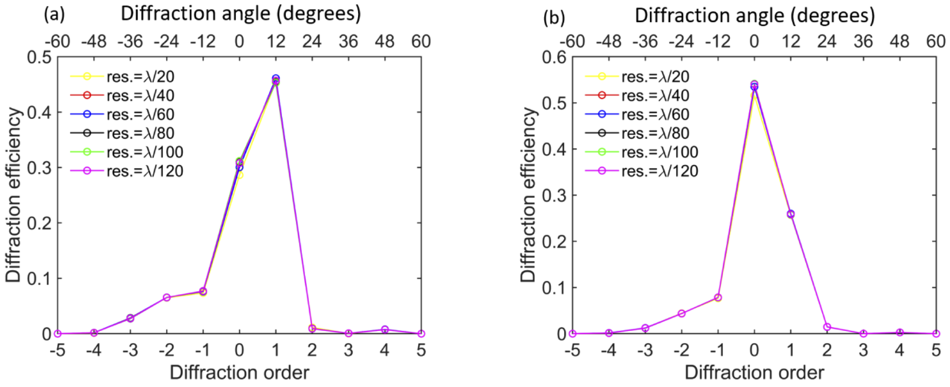

Fig. 7. Convergence analysis of the simulations (a) Probes attached, (b) Probes cleaved.

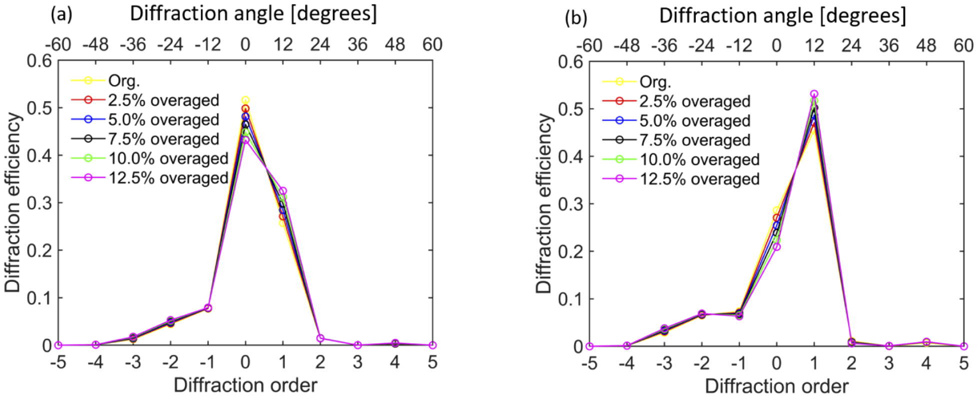

Fig. 8. Robustness analysis by intentionally introducing a fabrication error. It shows a reliable efficiency within 5 % fabrication error in overaged structure.

5.2. Robustness study

5.3. Phase of the Poynting vector

The x,y components of the Poynting vector field can be calculated with:

$$\mathbf{S}(x,y) = (S_x(x,y), S_y(x,y)) = \frac{1}{2}\,\mathrm{Re}\{\hat{\mathbf{E}}(x,y) \times \hat{\mathbf{H}}^*(x,y)\}, \tag{5}$$

where $\hat{\mathbf{E}}$ and $\hat{\mathbf{H}}$ represent the complex amplitude electromagnetic field. Then, the phase (ϕ_s) of the whole Poynting vector is defined as:

$$\sin(\phi_s) = \frac{S_y(x,y)}{|\mathbf{S}(x,y)|}, \cos(\phi_s) = \frac{S_x(x,y)}{|\mathbf{S}(x,y)|}. \tag{6}$$

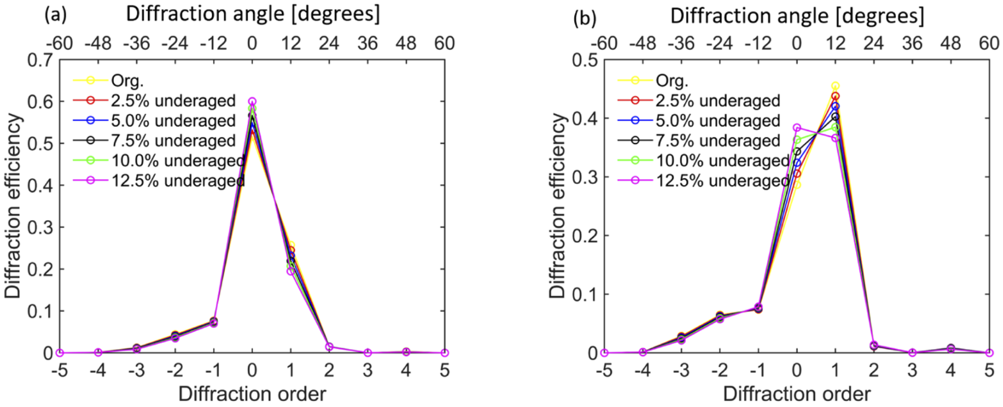

Fig. 9. Robustness analysis with intentionally introducing a fabrication error. It shows a reliable efficiency within 5 % fabrication error in underaged structure.

Table 1. Thickness parameters for a pre-optimized 1D Bragg reflector.

Layer label	Material	thickness (nm)
Layer1	SiO_2	115
Layer2	TiO_2	70
Layer3	SiO_2	115
Layer4	TiO_2	70
Layer5	SiO_2	115
Layer6	TiO_2	70
Layer7	SiO_2	115
Layer8	TiO_2	70
Layer9	SiO_2	115
Layer10	TiO_2	70

5.4. Geometrical parameters

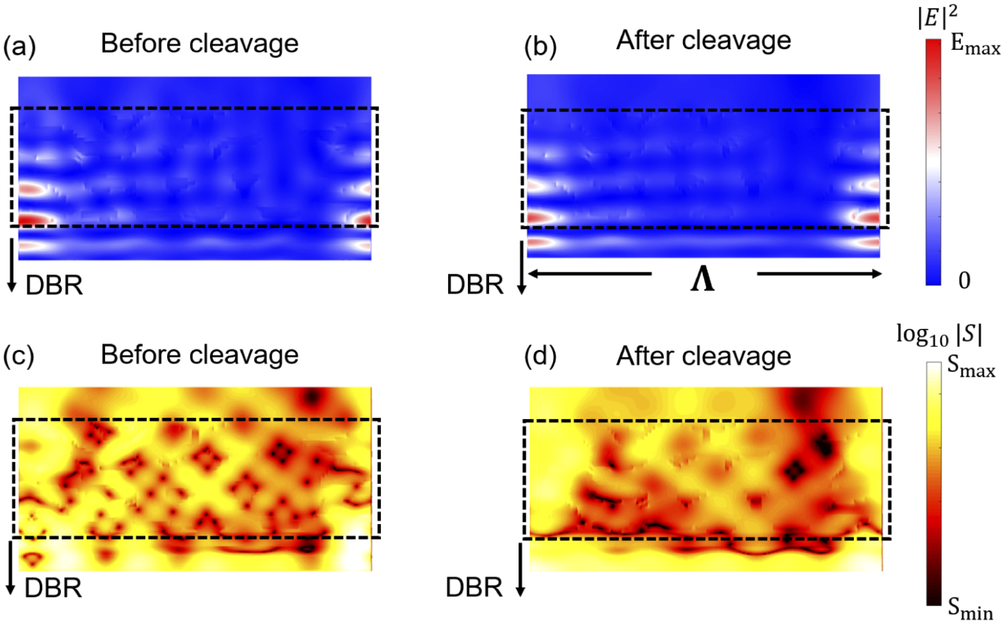

Fig. 10. Electric field intensity profile in near-field for (a) before cleavage (b) after cleavage of the optimized freeform structure. The absolute value of the Poynting vector in log scale for (c) before cleavage (d) after cleavage.

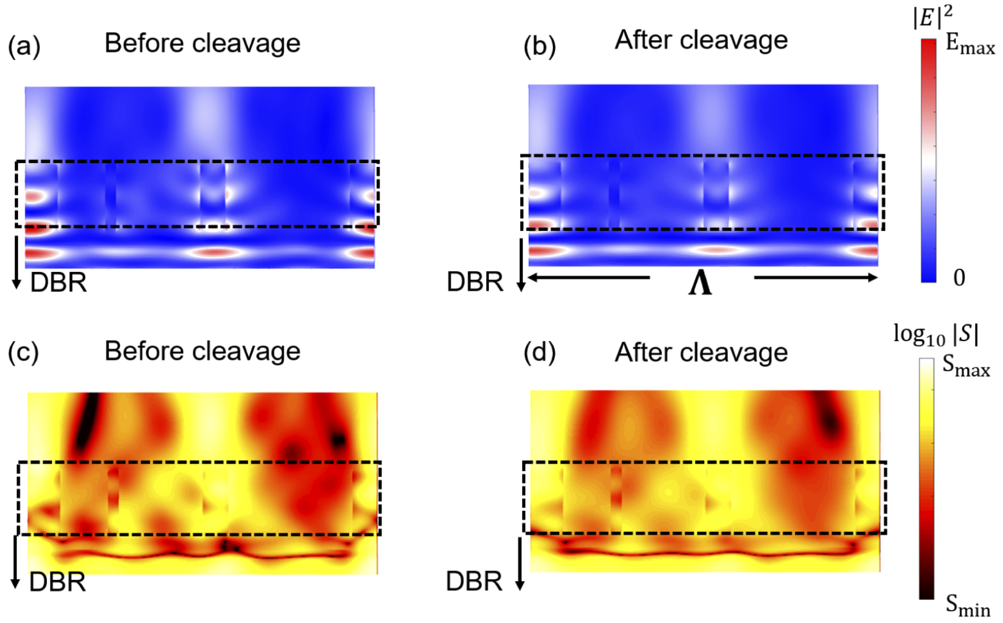

Fig. 11. Electric field intensity profile in near-field for (a) before cleavage (b) after cleavage of the optimized grating structure. The absolute value of the Poynting vector in log scale for (c) before cleavage (d) after cleavage.

Table 2. Geometry parameters for 2D freefrom biosensor. Each grid occupies 0.05λ length (30 nm) and 0.05λ height (30 nm) height. The value "1" means a functionalized PSi layer with Au-nanoparticle (NP)-labeled probes in state *a* and a functionalized PSi layer with cleaved Au-NP probes by the exposure to the target biomaterial in state *b*. The refractive index of "1" material is 1.2470 (state *a*) and 1.2849 (state *b*) when Au volume fraction is 1%, while the value "0" means freespace.

Grid number	
1	1 1 1 0 0 1 1 1 1 1 0 0 0 0 1 1 1 1 0 0 0 0 1 1 1 1 1 0 0 0 0
2	1 1 1 1 0 1 1 1 1 1 0 0 0 0 1 1 1 1 0 0 0 0 1 1 1 1 1 0 0 0 0
3	1 1 1 1 0 1 1 1 1 1 0 0 0 0 1 1 1 1 0 0 0 0 1 1 1 1 0 0 0 0 0
4	1 1 1 0 0 1 1 1 1 1 0 0 0 0 1 1 1 1 0 0 0 0 1 1 1 1 0 0 0 0 0
5	1 1 1 1 0 1 1 1 1 1 0 0 0 0 1 1 1 1 0 0 0 0 1 1 1 1 0 0 0 0 0
6	1 1 1 1 1 1 1 1 1 1 0 0 0 1 1 1 1 0 0 0 0 0 1 1 1 1 0 0 0 0 0
7	1 1 1 1 1 1 1 1 1 1 0 0 0 1 1 1 1 0 0 0 0 0 1 1 1 1 0 0 0 0 0
8	1 1 1 1 1 1 1 1 1 1 0 0 0 1 1 1 1 0 0 0 0 0 1 1 1 1 0 0 0 0 0
9	1 1 1 1 1 1 1 1 1 0 0 0 0 1 1 1 1 0 0 0 0 0 1 1 1 1 0 0 0 0 0
10	0 1 1 1 1 1 1 1 1 0 0 0 0 1 1 1 1 0 0 0 0 0 1 1 1 1 0 0 0 0 0
11	0 1 1 1 1 1 1 1 0 0 0 0 0 1 1 1 1 0 0 0 0 0 1 1 1 1 0 0 0 0 0
12	0 1 1 1 1 1 1 0 0 0 0 0 1 1 1 1 1 0 0 0 0 0 1 1 1 1 0 0 0 0 0
13	0 1 1 1 1 1 1 0 0 0 0 0 1 1 1 1 1 0 0 0 0 0 1 1 1 0 0 0 0 0 0
14	0 0 1 1 1 0 0 0 0 0 0 0 1 1 1 1 1 0 0 0 0 0 1 1 1 0 0 0 0 0 0
15	0 0 1 0 0 0 0 0 0 0 0 0 1 1 1 1 1 0 0 0 0 1 1 1 1 0 0 0 0 0 0
16	0 0 0 0 0 0 0 0 0 0 0 0 1 1 1 1 1 0 0 0 1 1 1 1 0 0 0 0 0 0 0
17	0 0 0 0 0 0 0 0 0 0 0 1 1 1 1 1 0 1 0 1 1 1 1 0 0 0 0 0 0 0 0
18	0 1 1 0 0 0 0 0 0 0 0 1 1 1 0 0 0 0 1 1 1 1 1 0 0 0 0 0 0 0 0
19	0 1 1 0 0 0 0 0 0 1 1 1 1 0 0 0 0 0 1 1 1 1 0 0 0 0 0 0 0 0 0
20	0 1 1 0 0 0 0 0 0 1 1 1 1 0 0 0 0 0 1 1 1 1 0 0 0 0 0 0 0 0 0
21	0 1 1 0 0 0 0 0 1 1 1 1 1 0 0 0 0 0 1 1 1 1 0 0 0 0 0 0 0 1 1
22	0 1 1 0 0 0 0 0 1 1 1 1 1 0 0 0 0 0 1 1 1 0 0 0 0 0 0 0 1 1 1
23	1 1 1 1 0 0 0 0 1 1 1 1 1 0 0 0 0 1 1 1 1 1 0 0 0 0 0 1 1 1 1
24	1 1 1 1 0 0 0 0 1 1 1 1 1 0 0 0 0 1 1 1 1 1 0 0 0 1 1 1 1 1 1
25	1 1 1 1 0 0 0 0 1 1 1 1 0 0 0 0 0 1 1 1 1 1 0 0 1 1 1 1 1 1 0
26	0 1 1 1 0 0 0 0 0 1 1 1 0 0 0 0 0 1 1 1 1 1 1 1 1 1 1 1 1 0 0
27	0 1 1 0 0 0 0 0 0 1 1 1 0 0 0 0 0 1 1 1 1 1 1 1 1 1 1 1 1 0 0
28	0 0 0 0 0 0 0 0 0 1 1 1 0 0 0 0 0 1 1 1 1 1 1 1 1 1 1 1 0 0 0
29	0 0 0 0 0 0 0 0 0 1 1 1 0 0 0 0 0 0 1 1 1 1 1 1 1 1 1 1 0 0 0
30	0 0 0 0 0 0 0 0 1 1 1 1 0 0 0 0 0 0 1 1 1 1 1 0 0 1 1 1 0 0 0
31	0 0 0 0 0 0 0 1 1 1 1 0 0 0 0 0 0 0 1 1 1 1 0 0 0 1 1 1 0 0 0
32	0 0 1 0 0 0 0 1 0 1 1 0 0 0 0 0 0 0 0 1 1 0 0 0 0 0 1 1 1 0 0
33	0 1 1 1 0 0 0 0 0 0 0 0 0 0 0 0 0 0 0 0 0 0 0 0 0 0 0 1 1 1 0
34	0 1 1 1 0 0 0 0 0 0 0 0 0 0 0 0 0 0 0 0 0 0 0 0 0 0 0 0 1 1 0
35	0 1 1 0 0 0 0 0 0 0 0 0 0 0 0 0 0 0 0 0 0 0 0 0 0 0 0 0 0 1 0
36	0 1 1 0 0 0 0 0 0 0 0 0 0 0 0 0 0 0 0 0 0 0 0 0 0 0 0 0 0 1 0

Grid number	
37	0 1 1 0 0 0 0 0 0 0 0 0 0 0 0 0 0 0 0 0 0 0 0 0 0 0 0 0 0 0 0
38	0 1 1 0 0 0 0 0 0 0 0 0 0 0 0 0 0 0 0 0 0 0 0 0 0 0 0 0 0 0 0
39	0 1 1 0 0 0 0 0 0 0 0 0 0 0 0 0 0 0 0 1 0 0 0 0 0 0 0 0 0 0 0
40	0 1 1 0 0 0 0 0 0 0 0 0 0 0 0 0 0 0 1 1 1 0 0 0 0 0 0 0 0 0 0
41	0 1 1 0 0 0 0 0 0 1 1 1 0 0 0 0 0 0 1 1 1 0 0 0 0 0 0 0 0 0 0
42	0 1 0 0 0 0 0 0 1 1 1 1 0 0 0 0 0 0 0 1 1 1 0 0 0 0 0 0 0 1 0
43	0 1 0 0 0 0 0 1 1 1 1 1 0 0 0 0 0 0 0 1 1 1 0 0 0 0 0 0 0 1 1
44	0 1 0 0 0 0 0 0 1 1 1 1 0 0 0 0 0 0 0 0 1 1 0 0 0 0 0 0 0 1 1
45	0 0 0 0 0 0 0 0 0 1 1 1 0 0 0 0 0 0 0 0 1 1 1 0 0 0 0 0 1 1 1
46	0 1 0 0 0 0 0 0 0 1 1 1 0 0 0 0 0 0 0 0 0 1 1 1 0 0 0 0 1 1 1
47	0 1 0 0 0 0 0 0 0 0 1 0 0 0 0 0 0 0 0 0 0 1 1 1 0 0 0 0 1 1 0
48	0 1 1 0 0 0 0 0 0 0 1 0 0 0 0 0 0 0 0 0 0 1 1 1 1 1 1 1 1 1 0
49	1 1 1 0 0 0 0 0 0 0 0 0 0 0 0 0 0 0 0 0 0 1 1 1 1 1 1 1 1 1 0
50	1 1 1 1 0 0 0 0 0 0 0 0 0 0 0 0 0 0 0 0 0 1 1 1 0 0 0 0 1 1 1
51	1 1 1 1 0 0 0 0 0 0 0 0 0 0 0 0 0 0 0 0 0 1 1 0 0 0 0 0 1 1 1
52	1 1 1 1 0 0 0 0 0 0 0 0 0 0 0 0 0 0 0 0 0 1 0 0 0 0 0 0 1 1 1
53	1 1 1 1 0 0 0 0 0 0 0 0 0 0 0 0 0 0 0 0 0 0 0 0 0 0 0 0 1 1 1
54	1 1 1 1 0 0 0 0 0 0 0 0 0 0 0 0 0 1 1 1 0 0 0 0 0 0 0 0 0 1 1
55	1 1 1 1 0 0 0 0 0 0 0 0 0 0 0 0 0 0 1 1 1 0 0 0 0 0 0 0 0 1 1
56	0 1 1 0 0 0 0 0 0 0 0 0 0 0 0 0 0 0 0 0 1 1 0 0 0 0 0 0 0 1 1
57	0 0 0 0 0 0 0 0 0 0 0 0 0 0 0 0 0 0 0 0 1 1 0 0 0 0 0 0 0 0 0
58	0 0 0 0 0 0 0 0 0 0 0 0 0 0 0 0 0 0 0 0 0 1 1 0 0 0 0 0 0 0 0
59	0 0 0 0 0 0 0 0 0 0 0 1 1 0 0 0 0 0 0 0 0 1 1 0 0 0 0 0 0 0 0
60	0 0 0 0 0 0 0 0 0 1 1 1 1 1 0 0 0 0 0 0 0 1 1 0 0 0 0 0 0 0 0
61	0 0 0 0 0 0 1 1 1 1 1 1 1 1 0 0 0 0 0 0 0 1 1 0 0 0 0 0 0 0 0
62	0 0 0 0 0 0 1 1 1 1 1 1 1 1 0 0 0 0 0 0 0 1 1 1 0 0 0 0 0 0 0
63	0 0 0 0 0 0 1 1 1 1 1 1 1 0 0 0 0 0 0 0 0 1 1 1 0 0 0 0 0 0 0
64	0 0 0 0 0 0 0 0 0 0 1 1 1 0 0 0 0 0 0 0 0 1 1 1 0 0 0 0 0 0 0
65	0 0 0 0 0 0 0 0 0 0 0 1 1 0 0 0 0 0 0 0 0 1 1 1 0 0 0 0 0 0 0
66	0 0 0 1 0 0 0 0 0 0 0 0 0 0 0 0 0 0 0 0 0 0 1 0 0 0 0 0 0 0 0
67	0 1 1 1 0 0 0 0 0 0 0 0 0 0 0 0 0 0 0 0 0 0 0 0 0 0 0 0 0 0 0
68	0 1 1 1 0 0 0 0 0 0 0 0 0 0 0 0 0 0 0 0 0 0 0 0 0 0 0 0 0 0 0
69	0 1 1 1 0 0 0 0 0 0 0 0 0 0 0 0 0 0 0 0 0 0 0 0 0 0 0 0 0 0 0
70	0 1 1 1 0 0 0 0 0 0 0 0 0 0 0 0 0 0 0 0 0 0 0 0 0 0 0 0 0 0 0
71	0 1 1 1 0 0 0 0 0 0 0 0 0 0 0 0 0 0 0 0 0 0 0 0 0 0 0 0 0 0 0
72	0 1 1 1 0 0 0 0 0 0 0 0 0 0 0 0 0 0 0 0 0 0 0 0 0 0 0 0 0 0 0
73	0 1 1 1 0 0 0 0 0 0 0 0 0 0 0 0 0 0 0 0 0 0 0 0 0 0 0 0 0 0 0
74	0 1 1 1 0 0 0 0 0 0 0 0 0 0 0 0 0 0 0 0 0 0 0 0 0 0 0 0 0 0 0
75	0 1 1 0 0 0 0 0 0 0 0 0 0 0 0 0 0 0 0 0 0 0 0 0 0 0 0 0 0 0 0

Grid number	
76	0 1 1 0 0 0 0 0 0 0 0 0 0 0 0 0 0 0 0 0 0 0 0 0 0 0 0 0 0 0 0
77	0 0 0 0 0 0 0 0 0 0 0 0 0 0 0 0 0 0 0 0 0 0 0 0 0 0 0 0 0 0 0
78	0 0 0 0 0 0 0 0 0 0 0 0 0 0 0 0 0 0 0 0 0 0 0 0 1 0 0 0 0 0 0
79	0 0 0 0 0 0 0 0 0 0 0 0 0 0 0 0 0 0 0 0 0 0 0 1 1 0 0 0 0 0 0
80	0 0 0 0 0 0 0 0 0 0 0 0 0 0 0 0 0 0 0 0 0 0 0 1 1 0 0 0 0 0 0
81	0 0 0 0 1 1 0 0 0 0 0 0 0 0 0 0 0 0 0 0 0 0 0 1 1 0 0 0 0 0 0
82	0 0 0 0 0 1 1 0 0 0 0 0 0 0 0 0 0 0 0 0 0 0 0 1 1 0 0 0 0 0 0
83	0 0 0 0 0 1 1 1 1 0 0 0 1 1 1 0 0 0 0 0 0 0 1 1 1 0 0 0 0 0 0
84	0 0 0 0 0 1 1 1 0 0 0 0 1 1 1 1 0 0 0 0 0 0 1 1 1 0 0 0 0 0 0
85	0 0 0 0 0 1 1 1 0 0 0 0 0 1 1 1 1 0 0 0 0 1 1 1 1 0 0 0 0 0 0
86	0 0 0 0 0 1 1 1 0 0 0 0 0 1 1 1 1 1 1 1 1 1 1 1 1 0 0 0 0 0 0
87	0 0 0 0 0 1 1 1 0 0 0 0 0 1 1 1 1 1 1 1 0 1 1 1 1 1 0 0 0 0 0
88	0 0 0 0 0 1 1 1 0 0 0 0 0 1 1 1 1 1 1 0 0 1 1 1 1 1 0 0 0 0 1
89	0 0 0 0 0 1 1 1 1 0 0 0 0 1 1 1 1 1 1 0 0 1 1 1 1 1 0 0 0 0 1
90	1 1 0 0 0 1 1 1 1 0 0 0 0 1 1 1 1 1 1 0 0 0 1 1 1 1 1 0 0 0 1
91	1 1 1 0 0 1 1 1 1 0 0 0 0 1 1 1 1 1 1 0 0 0 1 1 1 1 1 0 0 0 1
92	1 1 1 0 0 1 1 1 1 1 0 0 0 1 1 1 1 1 0 0 0 0 1 1 1 1 1 0 0 0 1
93	1 1 1 1 0 1 1 1 1 1 0 0 0 1 1 1 1 1 0 0 0 0 1 1 1 1 1 0 0 0 1
94	1 1 1 1 0 1 1 1 1 1 0 0 0 1 1 1 1 1 0 0 0 0 1 1 1 1 1 0 0 0 1
95	1 1 1 1 0 1 1 1 1 1 0 0 0 0 1 1 1 1 0 0 0 0 1 1 1 1 1 0 0 0 1
96	1 1 1 0 0 1 1 1 1 1 0 0 0 0 1 1 1 1 0 0 0 0 1 1 1 1 1 0 0 0 0

Table 3. Geometry parameters for 1D grating-based biosensor. Each grid occupies 0.05λ length (30 nm) and 0.9λ (540 nm) height. The value "1" means a functionalized PSi layer with Au-nanoparticle (NP)-labeled probes in state *a* and a functionalized PSi layer with cleaved Au-NP probes by the exposure to the target biomaterial in state *b*. The refractive index of "1" material is 1.2133 (state *a*) and 1.2849 (state *b*) when Au volume fraction is 2%, while the value "0" means freespace.

Grid number	Material									
1	0		25	0		49	0		73	0
2	0		26	0		50	0		74	0
3	1		27	0		51	1		75	0
4	1		28	0		52	1		76	0
5	1		29	0		53	1		77	0
6	1		30	1		54	1		78	1
7	1		31	1		55	0		79	1
8	0		32	1		56	0		80	1
9	0		33	1		57	0		81	1
10	0		34	1		58	0		82	1
11	0		35	1		59	0		83	1
12	0		36	1		60	0		84	1
13	0		37	1		61	0		85	1
14	0		38	1		62	0		86	1
15	0		39	1		63	0		87	1
16	0		40	1		64	0		88	1
17	0		41	1		65	0		89	1
18	0		42	1		66	0		90	1
19	0		43	1		67	0		91	1
20	0		44	1		68	0		92	1
21	0		45	1		69	0		93	1
22	0		46	1		70	0		94	1
23	0		47	0		71	0		95	0
24	0		48	0		72	0		96	0

Funding. U.S. Army Combat Capabilities Development Command Soldier Center (W911NF-13-D-0001).

Acknowledgements. The authors thank Michael Dubrovsky and Diedrik Vermeulen (SiPhox), Ke Du (Rochester Institute of Technology), Rabeb Layouni and Sharon M. Weiss (Vanderbilt University) for useful discussions. The authors also thank Owen D. Miller (Yale University) for providing insight and computational resources.

Disclosures. The authors declare no conflicts of interest.

References

1. C. Pacholski, M. Sartor, M. J. Sailor, F. Cunin, and G. M. Miskelly, "Biosensing using porous silicon double-layer interferometers: reflective interferometric fourier transform spectroscopy," J. Am. Chem. Soc. **127**(33), 11636–11645 (2005).
2. S. Ilyas, T. Böcking, K. Kilian, P. Reece, J. Gooding, K. Gaus, and M. Gal, "Porous silicon based narrow line-width rugate filters," Opt. Mater. **29**(6), 619–622 (2007).
3. C. Pacholski, "Photonic crystal sensors based on porous silicon," Sensors **13**(4), 4694–4713 (2013).
4. G. A. Rodriguez, S. Hu, and S. M. Weiss, "Porous silicon ring resonator for compact, high sensitivity biosensing applications," Opt. Express **23**(6), 7111–7119 (2015).
5. K. A. Kilian, T. Böcking, K. Gaus, M. Gal, and J. J. Gooding, "Peptide-modified optical filters for detecting protease activity," ACS Nano **1**(4), 355–361 (2007).

6. L. M. Bonanno and L. A. DeLouise, "Steric crowding effects on target detection in an affinity biosensor," Langmuir **23**(10), 5817–5823 (2007).
7. X. Wei and S. M. Weiss, "Guided mode biosensor based on grating coupled porous silicon waveguide," Opt. Express **19**(12), 11330–11339 (2011).
8. H. Qiao, B. Guan, J. J. Gooding, and P. J. Reece, "Protease detection using a porous silicon based bloch surface wave optical biosensor," Opt. Express **18**(14), 15174–15182 (2010).
9. C. Lv, Z. Jia, Y. Liu, J. Mo, P. Li, and X. Lv, "Angle-resolved diffraction grating biosensor based on porous silicon," J. Appl. Phys. **119**(9), 094502 (2016).
10. R. J. Martín-Palma, P. D. McAtee, R. Ramadan, and A. Lakhtakia, "Hybrid nanostructured porous silicon-silver layers for wideband optical absorption," Sci. Rep. **9**(1), 7291 (2019).
11. I. Rea, M. Iodice, G. Coppola, I. Rendina, A. Marino, and L. De Stefano, "A porous silicon-based bragg grating waveguide sensor for chemical monitoring," Sens. Actuators, B **139**(1), 39–43 (2009).
12. S. Arshavsky-Graham, N. Massad-Ivanir, E. Segal, and S. M. Weiss, "Porous silicon-based photonic biosensors: Current status and emerging applications," Anal. Chem. **91**(1), 441–467 (2019).
13. V. S. Lin, K. Motesharei, K. S. Dancil, M. J. Sailor, and M. R. Ghadiri, "A porous silicon-based optical interferometric biosensor," Science **278**(5339), 840–843 (1997).
14. S. Mariani, A. Paghi, A. A. La Mattina, A. Debrassi, L. Dahne, and G. Barillaro, "Decoration of porous silicon with gold nanoparticles via layer-by-layer nanoassembly for interferometric and hybrid photonic/plasmonic (bio) sensing," ACS Appl. Mater. Interfaces **11**(46), 43731–43740 (2019).
15. X. Lv, J. Mo, T. Jiang, F. Zhong, Z. Jia, J. Li, and F. Zhang, "Novel multilayered porous silicon-based immunosensor for determining hydroxysafflor yellow a," Appl. Surf. Sci. **257**(6), 1906–1910 (2011).
16. J. Goh, R. W. Loo, R. A. McAloney, and C. M. Goh, "Diffraction-based assay for detecting multiple analytes," Anal. Bioanal. Chem. **374**(1), 54–56 (2002).
17. M. Liscidini and J. Sipe, "Enhancement of diffraction for biosensing applications via bloch surface waves," Appl. Phys. Lett. **91**(25), 253125 (2007).
18. T. H. Talukdar, B. McCoy, S. K. Timmins, T. Khan, and J. D. Ryckman, "Hyperchromatic structural color for perceptually enhanced sensing by the naked eye," Proc. Natl. Acad. Sci. **117**(48), 30107–30117 (2020).
19. I. M. White and X. Fan, "On the performance quantification of resonant refractive index sensors," Opt. Express **16**(2), 1020–1028 (2008).
20. J. Hu, X. Sun, A. Agarwal, and L. C. Kimerling, "Design guidelines for optical resonator biochemical sensors," J. Opt. Soc. Am. B **26**(5), 1032–1041 (2009).
21. M. La Notte, B. Troia, T. Muciaccia, C. E. Campanella, F. De Leonardis, and V. Passaro, "Recent advances in gas and chemical detection by vernier effect-based photonic sensors," Sensors **14**(3), 4831–4855 (2014).
22. S. V. Boriskina and L. Dal Negro, "Self-referenced photonic molecule bio (chemical) sensor," Opt. Lett. **35**(14), 2496–2498 (2010).
23. L. Jason-Moller, M. Murphy, and J. Bruno, "Overview of biacore systems and their applications," Curr. protocols protein science **45**(1), 19 (2006).
24. J. D. Ryckman, M. Liscidini, J. Sipe, and S. M. Weiss, "Porous silicon structures for low-cost diffraction-based biosensing," Appl. Phys. Lett. **96**(17), 171103 (2010).
25. J. J. Amsden, H. Perry, S. V. Boriskina, A. Gopinath, D. L. Kaplan, L. Dal Negro, and F. G. Omenetto, "Spectral analysis of induced color change on periodically nanopatterned silk films," Opt. Express **17**(23), 21271–21279 (2009).
26. R. Layouni, M. Dubrovsky, M. Bao, H. Chung, K. Du, S. V. Boriskina, S. M. Weiss, and D. Vermeulen, "High contrast cleavage detection for enhancing porous silicon sensor sensitivity," Opt. Express **29**(1), 1–11 (2021).
27. M. Dubrovsky, M. Blevins, S. V. Boriskina, and D. Vermeulen, "High contrast probe cleavage detection," in *Laser Science*, (Optical Society of America, 2020), pp. JTu7C–3.
28. N. Majoul, S. Aouida, and B. Bessaïs, "Progress of porous silicon aptes-functionalization by ftir investigations," Appl. Surf. Sci. **331**, 388–391 (2015).
29. Z.-H. Wang and G. Jin, "Silicon surface modification with a mixed silanes layer to immobilize proteins for biosensor with imaging ellipsometry," Colloids Surf., B **34**(3), 173–177 (2004).
30. J. P. Broughton, X. Deng, G. Yu, C. L. Fasching, V. Servellita, J. Singh, X. Miao, J. A. Streithorst, A. Granados, A. Sotomayor-Gonzalez, K. Zorn, A. Gopes, E. Hsu, W. Gu, S. Miller, C.-Y. Pan, H. Guevara, D. A. Wadford, J. S. Chen, and C. Y. Chiu, "Crispr–cas12-based detection of sars-cov-2," Nat. Biotechnol. **38**(7), 870–874 (2020).
31. R. Bruch, J. Baaske, C. Chatelle, M. Meirich, S. Madlener, W. Weber, C. Dincer, and G. A. Urban, "Crispr/cas13a-powered electrochemical microfluidic biosensor for nucleic acid amplification-free mirna diagnostics," Adv. Mater. **31**(51), 1905311 (2019).
32. A. East-Seletsky, M. R. O'Connell, S. C. Knight, D. Burstein, J. H. Cate, R. Tjian, and J. A. Doudna, "Two distinct rnase activities of crispr-c2c2 enable guide-rna processing and rna detection," Nature **538**(7624), 270–273 (2016).
33. R. Drevinskas and P. G. Kazansky, "High-performance geometric phase elements in silica glass," APL Photonics **2**(6), 066104 (2017).
34. B. Reineke, B. Sain, R. Zhao, L. Carletti, B. Liu, L. Huang, C. De Angelis, and T. Zentgraf, "Silicon metasurfaces for third harmonic geometric phase manipulation and multiplexed holography," Nano Lett. **19**(9), 6585–6591 (2019).

35. T. Aoyagi, Y. Aoyagi, and S. Namba, "High-efficiency blazed grating couplers," Appl. Phys. Lett. **29**(5), 303–304 (1976).
36. F. Aieta, M. A. Kats, P. Genevet, and F. Capasso, "Multiwavelength achromatic metasurfaces by dispersive phase compensation," Science **347**(6228), 1342–1345 (2015).
37. N. Yu and F. Capasso, "Flat optics with designer metasurfaces," Nat. Mater. **13**(2), 139–150 (2014).
38. A. Ruiz-Clavijo, Y. Tsurimaki, O. Caballero-Calero, G. Ni, G. Chen, S. V. Boriskina, and M. Martín-González, "Engineering a full gamut of structural colors in all-dielectric mesoporous network metamaterials," ACS Photonics **5**(6), 2120–2128 (2018).
39. L. S. Pontryagin, V. G. Boltyanskii, R. V. Gamkrelidze, and E. F. Mishechenko, *The Mathematical Theory of Optimal Processes* (John Wiley & Sons, 1962).
40. J. Céa, A. Gioan, and J. Michel, "Quelques résultats sur l'identification de domaines," Calcolo **10**(3-4), 207–232 (1973).
41. O. Pironneau, *Optimal Shape Design for Elliptic Systems* (Springer-Verlag, 2012).
42. M. B. Giles and N. A. Pierce, "An Introduction to the Adjoint Approach to Design," Flow, Turbul. Combust. **65**(3/4), 393–415 (2000).
43. S. W. Director and R. A. Rohrer, "The Generalized Adjoint Network and Network Sensitivities," IEEE Trans. Circuit Theory **16**(3), 318–323 (1969).
44. M. P. Bendsoe and O. Sigmund, *Topology optimization: theory, methods, and applications* (Springer Science & Business Media, 2013).
45. A. Jameson, "Aerodynamic design via control theory," J. Sci. Comput. **3**(3), 233–260 (1988).
46. P. J. Werbos, *The Roots of Backpropagation* (John Wiley & Sons, Inc., 1994).
47. D. E. Rumelhart, G. E. Hinton, and R. J. Williams, "Learning representations by back-propagating errors," Nature **323**(6088), 533–536 (1986).
48. Y. LeCun, B. Boser, J. S. Denker, D. Henderson, R. E. Howard, W. Hubbard, and L. D. Jackel, "Backpropagation applied to handwritten zip code recognition," Neural Comput. **1**(4), 541–551 (1989).
49. C. M. Lalau-Keraly, S. Bhargava, O. D. Miller, and E. Yablonovitch, "Adjoint shape optimization applied to electromagnetic design," Opt. Express **21**(18), 21693–21701 (2013).
50. A. Y. Piggott, J. Lu, K. G. Lagoudakis, J. Petykiewicz, T. M. Babinec, and J. Vučković, "Inverse design and demonstration of a compact and broadband on-chip wavelength demultiplexer," Nat. Photonics **9**(6), 374–377 (2015).
51. L. Su, A. Y. Piggott, N. V. Sapra, J. Petykiewicz, and J. Vuckovic, "Inverse design and demonstration of a compact on-chip narrowband three-channel wavelength demultiplexer," ACS Photonics **5**(2), 301–305 (2018).
52. H. Men, K. Y. Lee, R. M. Freund, J. Peraire, and S. G. Johnson, "Robust topology optimization of three-dimensional photonic-crystal band-gap structures," Opt. Express **22**(19), 22632–22648 (2014).
53. D. Sell, J. Yang, S. Doshay, R. Yang, and J. A. Fan, "Large-angle, multifunctional metagratings based on freeform multimode geometries," Nano Lett. **17**(6), 3752–3757 (2017).
54. F. Callewaert, V. Velev, P. Kumar, A. Sahakian, and K. Aydin, "Inverse-designed broadband all-dielectric electromagnetic metadevices," Sci. Rep. **8**(1), 1358 (2018).
55. V. Ganapati, O. D. Miller, and E. Yablonovitch, "Light trapping textures designed by electromagnetic optimization for subwavelength thick solar cells," IEEE J. Photovoltaics **4**(1), 175–182 (2014).
56. H. Chung and O. D. Miller, "Tunable metasurface inverse design for 80% switching efficiencies and 144 angular deflection," ACS Photonics **7**(8), 2236–2243 (2020).
57. A. Taflove, A. Oskooi, and S. G. Johnson, *Advances in FDTD computational electrodynamics: photonics and nanotechnology* (Artech house, 2013).
58. O. D. Miller, "Photonic design: From fundamental solar cell physics to computational inverse design," Ph.D. thesis, University of California, Berkeley (2012).
59. A. F. Oskooi, D. Roundy, M. Ibanescu, P. Bermel, J. D. Joannopoulos, and S. G. Johnson, "Meep: A flexible free-software package for electromagnetic simulations by the fdtd method," Comput. Phys. Commun. **181**(3), 687–702 (2010).
60. E. D. Palik, *Handbook of optical constants of solids* (Academic, 1998).
61. R. G. Acres, A. V. Ellis, J. Alvino, C. E. Lenahan, D. A. Khodakov, G. F. Metha, and G. G. Andersson, "Molecular structure of 3-aminopropyltriethoxysilane layers formed on silanol-terminated silicon surfaces," J. Phys. Chem. C **116**(10), 6289–6297 (2012).
62. S. Kim, J. Chen, T. Cheng, A. Gindulyte, J. He, S. He, Q. Li, B. A. Shoemaker, P. A. Thiessen, B. Yu, L. Zaslavsky, J. Zhang, and E. E. Bolton, "Pubchem 2019 update: improved access to chemical data," Nucleic Acids Res. **47**(D1), D1102–D1109 (2019).
63. Y. Guo, J. Y. Ye, C. Divin, T. P. Thomas, A. Myc, T. F. Bersano-Begey, J. R. Baker Jr, and T. B. Norris, "Label-free biosensing using a photonic crystal structure in a total-internal-reflection geometry," in *Nanoscale Imaging, Sensing, and Actuation for Biomedical Applications VI*, vol. 7188 (International Society for Optics and Photonics, 2009), p. 71880B.
64. H. Chung and O. D. Miller, "High-na achromatic metalenses by inverse design," Opt. Express **28**(5), 6945–6965 (2020).
65. H. F. Schouten, T. D. Visser, and D. Lenstra, "Optical vortices near sub-wavelength structures," J. Opt. B: Quantum Semiclassical Opt. **6**(5), S404–S409 (2004).

66. M. Soskin, S. V. Boriskina, Y. Chong, M. R. Dennis, and A. Desyatnikov, "Singular optics and topological photonics," J. Opt. **19**(1), 010401 (2017).
67. M. R. Dennis, K. O'Holleran, and M. J. Padgett, "Singular optics: optical vortices and polarization singularities," Prog. Opt. **53**, 293–363 (2009).
68. S. V. Boriskina and N. I. Zheludev, *Singular and Chiral Nanoplasmonics* (CRC, 2014).
69. S. V. Boriskina and B. M. Reinhard, "Molding the flow of light on the nanoscale: from vortex nanogears to phase-operated plasmonic machinery," Nanoscale **4**(1), 76–90 (2012).
70. K. Li, M. I. Stockman, and D. J. Bergman, "Self-similar chain of metal nanospheres as an efficient nanolens," Phys. Rev. Lett. **91**(22), 227402 (2003).